Random vs realistic amorphous carbon models for high resolution microscopy and electron diffraction

C. Ricolleau, Y. Le Bouar, H. Amara, O. Landon-Cardinal, and D. Alloyeau

Citation: Journal of Applied Physics **114**, 213504 (2013); doi: 10.1063/1.4831669
View online: http://dx.doi.org/10.1063/1.4831669
View Table of Contents: http://scitation.aip.org/content/aip/journal/jap/114/21?ver=pdfcov
Published by the AIP Publishing

Random vs realistic amorphous carbon models for high resolution microscopy and electron diffraction

C. Ricolleau,[1,a)] Y. Le Bouar,[2] H. Amara,[2] O. Landon-Cardinal,[2,b)] and D. Alloyeau[1]
[1]*Laboratoire Matériaux et Phénomènes Quantiques, CNRS-UMR 7162, Université Paris Diderot-Paris 7, Case 7021, 75205 Paris Cedex 13, France*
[2]*Laboratoire d'Etude des Microstructures, UMR CNRS/Onera, 29, avenue de la Division Leclerc, 92322 Châtillon, France*

(Received 12 September 2013; accepted 31 October 2013; published online 3 December 2013)

Amorphous carbon and amorphous materials in general are of particular importance for high resolution electron microscopy, either for bulk materials, generally covered with an amorphous layer when prepared by ion milling techniques, or for nanoscale objects deposited on amorphous substrates. In order to quantify the information of the high resolution images at the atomic scale, a structural modeling of the sample is necessary prior to the calculation of the electron wave function propagation. It is thus essential to be able to reproduce the carbon structure as close as possible to the real one. The approach we propose here is to simulate a realistic carbon from an energetic model based on the tight-binding approximation in order to reproduce the important structural properties of amorphous carbon. At first, we compare this carbon with the carbon obtained by randomly generating the carbon atom positions. In both cases, we discuss the limit thickness of the phase object approximation. In a second step, we show the influence of both carbons models on (i) the contrast of Cu, Ag, and Au single atoms deposited on carbon and (ii) the determination of the long-range order parameter in CoPt bimetallic nanoalloys. © *2013 AIP Publishing LLC*.
[http://dx.doi.org/10.1063/1.4831669]

I. INTRODUCTION

Thanks to the developments of aberration correctors in electron microscope, it is now possible to push the limit of ultra high resolution imaging and to resolve very small interatomic distances as well as to detect single atoms on surface or in interstitial position.[1–5] Difficulties arise when one wants to extract quantitative data from these informative images. The widely used methodology for images quantification is to compare experimental images with simulated ones obtained with a model, as realistic as possible, of the material under investigation.[6,7]

In this context, amorphous materials play a significant role because they are present in many sample configurations. For Transmission Electron Microscopy (TEM) observations, samples are very often prepared by ion milling techniques. These methods generate amorphous layer on both free surfaces of the specimen. Amorphous substrates (C, Ge, Si_3N_4, SiO_2, etc.) are also commonly used to support single nanostructures such as nanoparticles (NPs), nanowires, nanotube, etc.

Up to now, to model amorphous systems for the simulations of high resolution electron microscopy (HRTEM) images, two techniques are mainly used. The simplest model consists in the random generation of the atom positions inside a simulation box in which the atomic density is controlled.[8,9] The other commonly used approach is to directly model the wave function emerging from the amorphous specimen by assuming that the phases in the Fourier transform of the projected potential can be treated approximately as a random variable (Random Phase Approximation method).[10–12] This approach is, however, based on several assumptions. First, the correlation distance of the atomic positions has to be much smaller than the layer thickness. Then, this approach relies on the weak phase approximation and on the projected potential approximation. It has been shown that these approximations induce significant errors on the propagation of phase shifts within the material.[13] Finally, simplifying assumptions have to be made on the standard deviation of the random variable and on its dependence on the layer thickness. Note that the Random Phase Approximation has been extended to include the consequences of the correlations of atomic positions on the diffracted intensities.[11]

These approaches are only associated with a very poor description of the structure of the amorphous material, ignoring chemical bond distances and angles and also the coordination numbers. Indeed, diamond consists of four-coordinate carbon atoms with tetrahedral geometry, while graphene and carbon nanotubes involve three-coordinate carbon atoms and two-coordinate carbon atoms in case of linear chains. All these geometrical properties are crucial to reproduce correctly the main physical properties of amorphous carbon structures where sp, sp^2, and sp^3 bonds are present. It has thus been proposed to use Continuous Random Network[14] to improve the structural description of the amorphous material used for simulating HRTEM images, but this geometrical model fails to reproduce the medium range correlations.[15]

In this paper, we propose a new method to model in a more realistic way amorphous carbon (a-C) that accurately accounts for its 3D structure. It is based on an energetic

[a)]Electronic mail: Christian.Ricolleau@univ-paris-diderot.fr.
[b)]Currently address: Département de Physique, Université de Sherbrooke, Sherbrooke, Québec J1K 2R1, Canada.

approach with a tight-binding (TB) potential in which the electronic band structure of the material is calculated with the recursion technique.[16] The main advantage of this model is that it gives a very good description of the *sp*, sp^2, and sp^3 hybrid bonds and their competition.

In the first part, the model and the main properties of the generated carbon are presented. Then, the structural properties of this carbon and the one generated with random atomic positions are compared. In all cases, we discuss the behavior of both the phase and the amplitude of the transmitted beam as a function of the thickness. Finally, we show how both carbons influence (i) the contrast of single atoms deposited on a-C on high resolution imaging and (ii) the determination of the long-range order parameter in bimetallic nanoalloys from electron diffraction pattern.

II. AMORPHOUS CARBON MODELING

A. Tight-binding model

Due to the technological importance of carbon, a large number of potentials has been proposed in the literature to model its cohesive properties. One of the first reactive potentials was developed by Stillinger and Weber who proposed a simple model for silicon[17] also applied to carbon.[18] An important contribution for covalent materials was made by Tersoff, who introduced a so-called bond-order-potential (BOP) for silicon[19] which was parametrized later also for carbon[20] and more recently improved with a long-range interaction.[21] Nowadays, there exist also reactive potentials, such as ReaxFF potentials[22] where the total energy is the sum of various more or less independent contributions. All these methods are very useful for studying large systems (several thousand of atoms) during a long time scale (a few tens of nanoseconds).

A second popular class of potentials has been derived in the framework of a tight-binding approximation, which is perfectly adapted to provide very good descriptions of the electronic structure and of the energies of carbon covalent bonds.[23–25] Although in principle more transferable than empirical models, tight-binding models also depend on adjustable parameters to build the Hamiltonian matrix of the interactions and to describe the empirical term that is always present. These parameters are usually fitted to *ab initio* or experimental data when they exist.

In the present study, the interaction between carbon atoms is treated within the semi-empirical tight-binding approach described in Ref. 16 derived from the model introduced by Xu *et al.*[23] Both *s* and *p* electrons are taken into account, with the corresponding *s*, p_x, p_y, and p_z atomic orbitals. The total energy of the system is split in two parts, a band term that describes the formation of an energy band when atoms are put together and a repulsive term that empirically accounts for the ionic and electronic repulsions. It is convenient to decompose these terms into local contributions for each atom *i*, so that

$$E^i_{tot} = E^i_{band} + E^i_{rep}. \tag{1}$$

The total energy of the system, E_{tot}, then writes

$$E_{tot} = \sum_i E^i_{tot}. \tag{2}$$

The band term energy, E_{band}, is given by

$$E^i_{band} = \int_{-\infty}^{E_F} (E - \varepsilon^0_i)\, n_i(E)\, dE, \tag{3}$$

where E_F is the Fermi level and ε^0_i is the atomic energy level. Instead of performing a diagonalization of the Hamiltonian matrix, we use the recursion method to calculate the local electronic density of states $n_i(E)$ on each site.[26] Only the first four continued fraction coefficients corresponding to the first four moments of the local density of states are calculated exactly. This is the minimal approximation that takes into account the directional character of the carbon $s-p$ bond. As compared to the standard diagonalization technique, this approach, of order *N*, is particularly useful for the study of large and fully relaxed systems. For the repulsive part of the energy, we use also the form proposed by Xu *et al.*,[23]

$$E^i_{rep} = F\left[\sum_{j\neq i} \phi(r_{ij})\right], \tag{4}$$

where $F(x)$ is a polynomial function and $\phi\,(r_{ij})$ is a repulsive pairwise potential.

In these conditions, for C-C interactions, the tight-binding parameters have been fitted in order to reproduce accurately the competition between *sp*, sp^2, and sp^3 atomic arrangements.

In all cases, the model is fairly accurate when compared to experiment or to *ab initio* calculations indicating its good transferability.[16] Indeed, the model is shown to reproduce several properties such as the diamond to rhombohedral-graphite transition or the energy of local defects present in carbon structures. Due to the use of a complete (*s*,*p*) basis for carbon states, all types of covalent sp^n bonds present in graphene, a nanotube or a three-dimensional amorphous C phase can be modeled.

This energetic model, both simple and accurate, is then implemented in a Monte Carlo code (MC) using either a canonical or a grand canonical (GC) algorithm with fixed volume, temperature, and C chemical potential μ_C.[27] In our simulations, C atoms can be incorporated everywhere in the box with a thermodynamic acceptance criterion. This approach is perfectly adapted to generate realistic configurations with different local environments (*sp*, sp^2, or sp^3) depending on the temperature and the carbon chemical potential. Then the final configurations are obtained by performing relaxations in the canonical ensemble (at fixed number of C atoms). Furthermore, recent technical improvements of the algorithm of our tight-binding Monte Carlo code made it significantly faster.[28] The exploration of longer time scales and more extensive investigations is then possible.

More precisely, we generate a number of amorphous carbon structures with various sizes, by first performing GCMC simulations at 2000 K. Such structures result from the growth conditions: the carbon chemical potential is chosen to be very high: we use values around −3.00 eV/atom which are significantly higher than the cohesive energies of the various carbon phases (e.g., −7.41 eV/atom for a graphene

layer in our model). Under such particular conditions (T and μ_C), the growth is too fast and defects have a very high probability to be formed. Then, the final atomistic configurations, considered below as substrate for HRTEM image simulations, are obtained by performing a simulated annealing. In this process, the atomic configuration, initially at 2000 K, is slowly cooled down so that the system is in thermodynamic equilibrium at every step. In this way, we created a number of carbon amorphous structures with a density around $2.20\,g\times cm^{-3}$,[29] i.e., slightly lower than the one for graphite, in boxes ranging from $5\times5\times1$ nm^3 to $5\times5\times5\,nm^3$ corresponding to 3000 and 13 000 atoms, respectively. As seen in Fig. 1(a), final structures consist of rings (hexagons, pentagons, heptagons, etc.), linear chains, isolated C atoms and pores as already described in Ref. 30.

If a very thick amorphous layer is needed, the computational time becomes prohibitive. The way to circumvent this limitation is to combine as "building blocks" several simulation boxes obtained independently with the TB potential. This approach is of course only valid if the blocks thickness is significantly larger than the correlation distance in the material. In addition, when thickness as thick as 50 nm is needed, it is necessary to use several times the same building block. In that case, the blocks are randomly shifted and rotated in order to avoid spurious fluctuations in the simulated HRTEM images.[9] The x, y, z positions of the C atoms for $5\times5\times1\,nm^3$, $5\times5\times3\,nm^3$ and $5\times5\times5$ nm^3 building blocks calculated for different initial configurations are given in supplementary materials.[31]

B. Random carbon model

The amorphous carbon layers generated randomly are obtained by placing C atoms with random positions within the volume of the layer, to reach a density of $2.2\,g\times cm^{-3}$. During this procedure, a new carbon atom is included in the structure only if its distance with all existing atoms is above a minimal distance chosen equal to 0.14nm, i.e., slightly lower than the C-C bond length of 0.142 nm in graphene. The resulting projected image of the a-C layer structure is shown in Fig. 1(b) and compared with the one generated in the tight-binding framework (Fig. 1(a)). It can be observed that the 3D atomic configurations are very different since characteristic features of a real amorphous carbon structure such as hexagonal and pentagonal arrangements of atoms are only visible in the TB carbon.

The correlation of the atom positions also strongly differ between the two types of carbon as evidenced by the 3D radial distribution function (RDF) presented in Fig. 1(c). Indeed, the RDF of the TB amorphous structure displays strong peaks related to the first and second nearest neighbour distances, while the RDF of the random amorphous carbon is flat.

III. PHASE AND AMPLITUDE VARIATION OF THE TRANSMITTED BEAM IN RANDOM AND TIGHT-BINDING CARBONS

The propagation of an electronic plane wave through a layer of amorphous carbon is presented in this section for both the random and TB models.

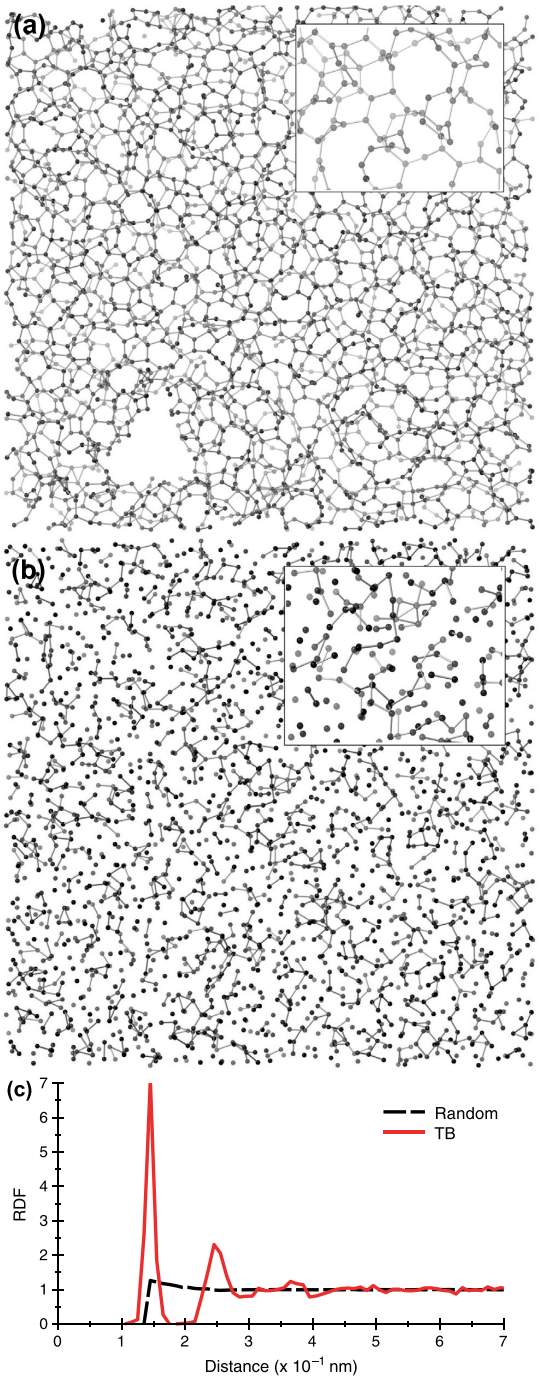

FIG. 1. 3D perspective view of the carbon generated by: (a) tight-binging model and (b) random model. The thickness of the box corresponding to these two projected structures is 1 nm. (c) 3D radial distribution functions (RDF) of carbon atomic positions generated by tight-binding (red) and random (black) models.

In this work, dynamical theory calculations are performed using a commercial (JEMS[32]) and a homemade software (NanoTEM). We have used the multislice approach[33] using the scattering factors given by Peng. *et al.*[34] In our calculations, the projected potential inside a slice is due not only to the atoms inside the slice but also to the atoms in the neighboring slice. When considering amorphous materials, this point may be important because many atoms are located close to the plane separating two slices and therefore contribute to potential in these two slices. When HRTEM images

are computed, aberration coefficients of a new generation aberration-corrected microscope, the JEM-ARM-200F are used.[35] Spherical and chromatic aberration coefficients are $C_s = 2\,\mu m$ and $C_c = 1\,mm$, respectively, two-fold astigmatism $< 1\,nm$, defocus spread $= 2.2\,nm$ and a half convergence angle of 1 mrad. All images are computed at 200 kV, using a Scherzer defocus $\Delta f = -2.74\,nm$, and absorption and Debye Waller factors are neglected.

Fig. 2 presents the evolution of the transmitted beam (i.e., the unscattered part of the electron wave) through the two types of amorphous carbon. Fig. 2(a) demonstrates that, in both cases, the phase linearly increases with the layer thickness, and that the increase rate is equal to the one predicted by the phase object approximation in which the potential within the layer is replaced by its average value. By introducing the electron scattering length for carbon $f_C^e(0)$ and the average atomic density ρ_V the phase can be expressed as

$$\phi = \lambda\,\gamma\,\rho_V f_C^e(0)\,\Delta z, \tag{5}$$

where λ is the electron wavelength, γ the relativistic coefficient and Δz the layer thickness. It means that the phase of the transmitted beam is not sensitive to the details of the amorphous structure but only to the atomic density of the carbon layer.

The evolution of the intensity of the transmitted beam is shown in Fig. 2(b). In the random and TB amorphous structures, the intensity linearly decreases with the layer thickness, but the decrease rate is smaller with the random structure. A 10% decrease of the intensity is obtained for a 21 nm thickness of TB carbon but requires 27 nm with the random structure. Hence, if we define a critical thickness for the validity of the phase object approximation using the transmitted beam intensity, this critical thickness is about 30% overestimated if a random amorphous is used.

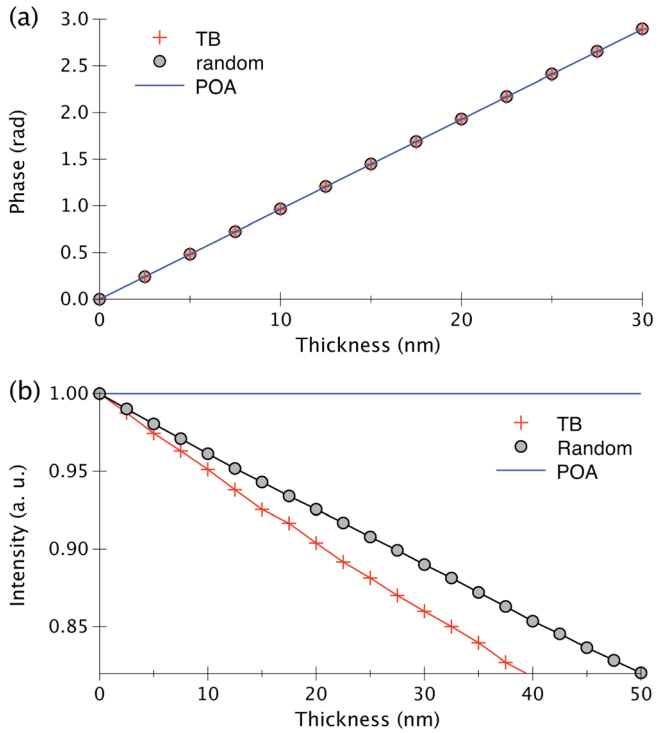

FIG. 2. Comparison of the (a) phase and (b) intensity of the transmitted beam (i.e., the unscattered part of the electron wave) calculated using Random and TB carbon structures as a function of the thickness layer. The slice thickness is 0.25 nm. The simulation box size in the layer plane is 5 nm × 5 nm with a 1024 × 1024 sampling.

The link between the atomic structure and the evolution of the wave function can also be analyzed analytically. The way to proceed is to divide the electrostatic potential $V(\vec{r})$ inside the amorphous layer into a homogeneous potential $\bar{V}$, equal to the spatial average of the true potential, and a heterogeneous part $\delta V(\vec{r}) = V(\vec{r}) - \bar{V}$. Then, assuming that the heterogeneous part of the potential is smaller than the homogeneous one, the propagation of the wave function can be obtained by a perturbation expansion.[36] Only the main results are discussed in this section. Details of the calculations are given in Appendix A.

Assuming that the incident beam is a plane wave of amplitude Ψ_i and wave vector k_z along the z axis, the solution of the time-independent elastic scattering equation is, to the zeroth order:

$$\Psi^{(0)}(\Delta z) = \Psi_i \exp(-i\gamma_0\,\Delta z), \tag{6}$$

where $\gamma_0 = \bar{V}/(2k_z)$, and where the fast oscillating term $\exp(ik_z\,\Delta z)$ is omitted for clarity. Note that this expression corresponds to the wave function obtained within the phase object approximation, in which the potential has been approximated by its average value. At zeroth order, we therefore recover the phase shift given by Eq. (5) and the ones observed in both the random and TB amorphous carbon layers.

As shown in the appendix, the perturbation expansion to the second order within the projected potential approximation predicts a decrease of the transmitted beam intensity given by

$$I_{q=0} \approx 1 - (\Delta z)^2 \sum_{\vec{q}\neq 0} \mathrm{sinc}^2\left(\frac{q^2\Delta z}{4\,k_z}\right) \hat{\Gamma}^{\Delta z}(\vec{q})\,|\hat{\mathcal{V}}_p^{at}(q)|^2, \tag{7}$$

where $\hat{\Gamma}^{\Delta z}$ is the 2D correlation function of the atoms positions in the layer and where $\hat{\mathcal{V}}_p^{at}(q)$ is the Fourier transform of the projected potential of a single atom. Because, for not too thick layers, the sinc function may be replaced by 1 and because $\hat{\Gamma}^{\Delta z}$ scales as $1/\Delta z$ (see appendix for detailed explanation) we predict a decrease of the transmitted beam intensity which is almost linear with the layer thickness, as observed in Fig. 2(b). More importantly, we show that the decrease rate is directly related to the amorphous carbon structure through the atoms positions correlations. Therefore, these correlations in the TB amorphous carbon, evidenced by the strong peaks in the RDF, explain the faster decrease of the transmitted beam intensity when compared to the random carbon.

IV. INFLUENCE OF THE CARBON STRUCTURE ON THE CONTRAST OF SINGLE ATOMS IMAGING

To understand nanomaterials fabrication, the growth of nanoparticles on surfaces or any physical mechanisms

involved in the transport of matter during NPs coarsening, such as Ostwald ripening[37–39] or coalescence,[40–43] one has to observe single atoms on surface. More importantly, when nanomaterials are constituted of more than one element, such as metallic and semiconductor nanoalloys, it is of primary importance to determine the chemical nature of the diffusing atoms on the substrate. This identification allows to understand the origin of the possible compositional change of the nanoalloys due to the non homogeneous exchange of atoms during heat treatments.[1,37]

The aim of this section is to quantify the signal to noise ratio (SNR) of the contrast of single Cu, Ag, and Au atoms deposited on amorphous carbon by using HRTEM imaging. We used the SNR definition proposed by Rose[44] to quantify the simulated contrast of these single atoms in the HRTEM images. The SNR is calculated by using the following relation:

$$\mathrm{SNR} = \frac{I - I_0}{\sigma}, \tag{8}$$

where I is the intensity value at the atom position, I_0 is the mean intensity in the carbon layer only area, i.e., the signal is defined as the incremental change in the image intensity due to the atom and σ is the standard deviation of I_0.

The atomic models used for the simulation consist in a 5 nm thick amorphous carbon layer on which 24 atoms of Cu, Ag, and Au are placed on different positions on the a-C substrate. The Cu atoms are positioned on the first three columns at $x = 0.150$, 0.250, and 0.320, respectively, the Ag atoms are in the 3 following columns at $x = 0.430$, 0.500, and 0.570 and the Au ones are placed on the last three columns at $x = 0.680$, 0.750, 0.850. These atoms have been chosen because they show a large difference in their atomic numbers. We choose to measure the intensity on several atoms to obtain a statistical value of the SNR. For the a-C substrate, we use the random and the tight-binding models to generate the positions of C atoms inside five stacked $5 \times 5 \times 1\,\mathrm{nm}^3$ simulation boxes. A 1024×1024 pixel^2 image size was used for the simulations so as to ensure a real space sampling of $0.005\,\mathrm{nm.pixel}^{-1}$ in both the x and y directions.

In the multislice method used for the HRTEM image simulations, the slice thickness along the beam direction was 0.25 nm. The defocus value ($\Delta f = -2.74$ nm) was chosen in order to maximize the contrast and in a range of focus where the variations of the SNR of single atoms contrast is almost constant.[1] In such defocus condition, the contrast of the atoms is black. The SNR was calculated by measuring the minimum of the intensity in a small 64 pixels $\times$ 64 pixels box centered on the position of the atoms when they are visible on the HRTEM images. In the case of copper atoms, the SNR was calculated on the atoms which are visible on the HRTEM image. The σ values determined on these SNR are thus less significant than the ones obtained for Ag and Au atoms since they have been calculated on smaller data sets.

The resulting HRTEM images for both random and tight-binding carbon films are shown on Figs. 3(a) and 3(b), respectively. The values of the SNR of the intensity contrast, and its standard deviation σ, for Cu, Ag, and Au single atoms deposited on the two carbon substrates (random and tight-binding ones) are given in Table I.

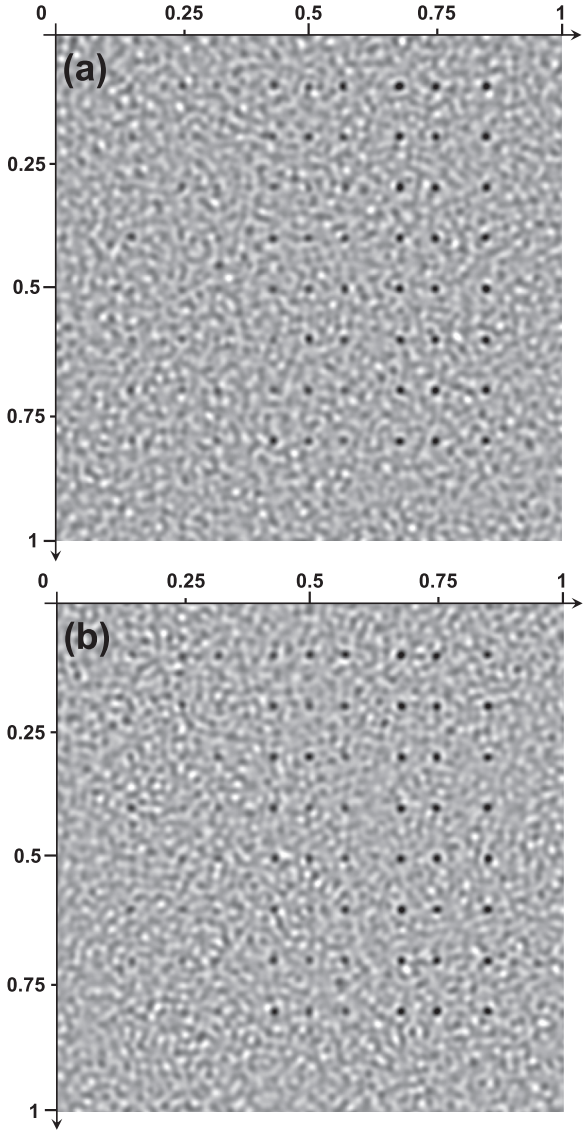

FIG. 3. Comparison of the bright field HRTEM images of Cu, Ag and Au atoms deposited on 5 nm thick amorphous layer calculated by (a) random atomic positions generation and (b) using the tight-binding model approximation. The Cu atoms are positioned on the first three columns, the Ag atoms are in the 3 following ones and the Au ones are placed on the last three columns.

The absolute value of the SNR increases as a function of the atomic number while the standard deviation decreases. This behavior is consistent with the atomic potential becoming deeper when increasing the Z number of the atom by

TABLE I. Value of the SNR of the intensity contrast and its standard deviation σ for Cu, Ag, and Au single atoms deposited on amorphous carbons generated with the random and the tight-binding models.

		Cu	Ag	Au
Random carbon	SNR	− 4.74	− 5.84	− 7.23
	σ	0.65	0.78	0.67
TB carbon	SNR	− 5.15	− 6.53	− 8.23
	σ	0.75	1.36	1.25

comparison to the mean atomic potential of amorphous carbon. On both types of carbons, there is an overlap between the SNR ranges of the 3 atoms due to a fairly high standard deviation. It is thus not possible to distinguish unambiguously Cu from Ag and Ag from Au whereas Cu and Au can be clearly distinguished if they coexist on a surface.

The standard deviation of the SNR of all 3 atoms is higher for TB carbon than for random carbon substrate. This effect may be explained by the porosities which are generated in the TB model (see Fig. 1(a)) and which are missing in the random amorphous. However, a detailed analysis of the value of the standard deviation of the SNR and its link with the existence of pores remains to be done.

Finally, we note that, in Table I, the mean values of SNR of the atoms are slightly higher for TB carbon. However, due to the large standard deviation values, this difference is not statistically meaningful. The origin of these large values relies on the local density fluctuations of the underlying a-C layer. Indeed, for small a-C thicknesses, the projected density varies rapidly from one area to another. It is then possible to observe important variations in the intensity of the single atoms depending on its position on the a-C substrate if the number of measurements is small. The fluctuations of the local density become less and less important as the thickness of the a-C substrate increases and this effect becomes less significant for larger a-C thicknesses. We may wonder if the SNR measurements on a larger number of atom positions could reveal a statistically relevant difference between the random and TB amorphous layers. To analyze this point, we have performed measurements for more than 2000 positions of a Au atom. We have found that, with this large set of measurements, no significant difference can be observed between the values of the SNR on the two types of amorphous carbon. This conclusion can be interpreted by using the following simple approach.

Within the weak phase approximation, it can be shown that the intensity measured in a HRTEM image at the atom position is equal to the intensity that would have occurred without the atom multiplied by a coefficient which depends on the atom type. This coefficient, which depends on the atomic scattering factor, can be easily measured by propagating a plane wave on a single atom without substrate. Since the a-C generated using both models have the same density, they must have the same mean projected potential and the mean amplitude of the exit wave functions have to be identical. Numerically, we obtain $I_0 = 0.9932 \pm 0.0758$ for random carbon and $I_0 = 0.9931 \pm 0.0748$ for tight-binding carbon. Since this wave function acts as the incident wave on the single atoms, no differences have to be observed on the mean intensity of a given atom between the two carbon models.

V. INFLUENCE OF THE CARBON STRUCTURE ON THE DETERMINATION OF LONG-RANGE ORDER PARAMETER IN BIMETALLIC NANOPARTICLES

While huge progress have been done in the understanding of growth and structural properties of bimetallic nanoparticles (NPs), the phase diagram of such nanoalloys and the nature of phase transitions are still open questions. In particular, for order/disorder transitions, the quantitative study of the transitions requires the determination of the long range order (LRO) parameter as a function of temperature and particle size. The measurement of the LRO can be done using X-ray diffraction on a NP assembly but in that case no link between the size and the value of the LRO can be made except for perfectly monodisperse NP assemblies which are experimentally difficult to obtain, especially for NPs grown from vapor phase deposition techniques. While some attempts have been done by using HRTEM imaging,[45] the best technique to determine the LRO on single nanoparticles is electron diffraction in a TEM. Chemical ordering is a thermally activated process that induces the apparition of superstructure reflections on diffraction patterns in addition to the fundamental reflections coming from the diffraction of the face centered cubic (FCC) lattice of the high temperature phase. Sato *et al.* and Miyazaki *et al.* have shown that it is possible to determine the LRO on bimetallic NPs by using the intensity ratio of superstructure and fundamental reflections, I_S and I_F, respectively, when the NPs are oriented in kinematical diffraction conditions.[46–48]

In dynamical diffraction conditions, it is more trickier to determine the LRO. Indeed, diffracted intensities depend strongly on the NPs thickness and their orientations with respect to the electron beam. The ratio I_S/I_F is then no longer proportional to the square of the LRO parameter. In such a case, the determination of the LRO can be done by comparing the experimental I_S/I_F ratios measured by electron diffraction to diffraction simulations obtained from structural models where the orientation and the thickness of the NPs are fixed and for different known values of the LRO.

In this section, we investigate the importance of the choice of the structural model of the amorphous substrate when measuring the LRO parameter of a supported NP. For this purpose, we choose the CoPt system which has been extensively studied both experimentally[6,45,49–51] and theoretically.[52–55] In this system, stoichiometric alloys are ordered at low temperature in the $L1_0$ structure. This ordered structure is built on an underlying FCC lattice and can be described as the stacking of alternatively cobalt-rich and platinum-rich planes along the [001] direction. The LRO parameter is defined by the difference in platinum composition of two successive planes.

The $4.862 \times 4.862 \times 10$ nm^3 boxes of amorphous carbon were generated using both random and TB carbon models. The size of the simulation box is chosen to be a multiple of the CoPt unit cell parameter (0.374 nm). In this case, the diffracted peaks of the CoPt nanoparticle coincide exactly with one point of the sampling of the Fourier space. This ensures a rapid convergence of the results with the number of sampling points and facilitates the measurement of the intensity of the peaks.

A CoPt NP of 3 nm in size and oriented along the [001] zone axis was placed at the bottom of the simulation boxes. Two values for the LRO have been considered: 0.4 and 0.8. For each configuration, electron diffraction pattern were calculated by using the multislice technique with a slice thickness of 0.187 nm, i.e., the distance between the (002) planes of the CoPt FCC structure and using the same optical parameters as those given in Sec. III.

The intensity profiles for both the 110 superstructure and the 220 fundamental reflections are shown on Fig. 4 for the CoPt nanoparticle only, the NP deposited on a 10 nm thick random and TB amorphous carbon layer and for both values of the LRO, 0.4 and 0.8.

The values of the intensity of the 110, the 220 reflections, and the value of the I_S/I_F ratio for the 6 configurations are given in Table II. The intensity of the 220 reflection is almost not sensitive to the carbon model meaning that for high spatial frequencies, both carbons have the same behavior. On the opposite, the intensity value of the 110 reflection depends fairly strongly on the carbon model.

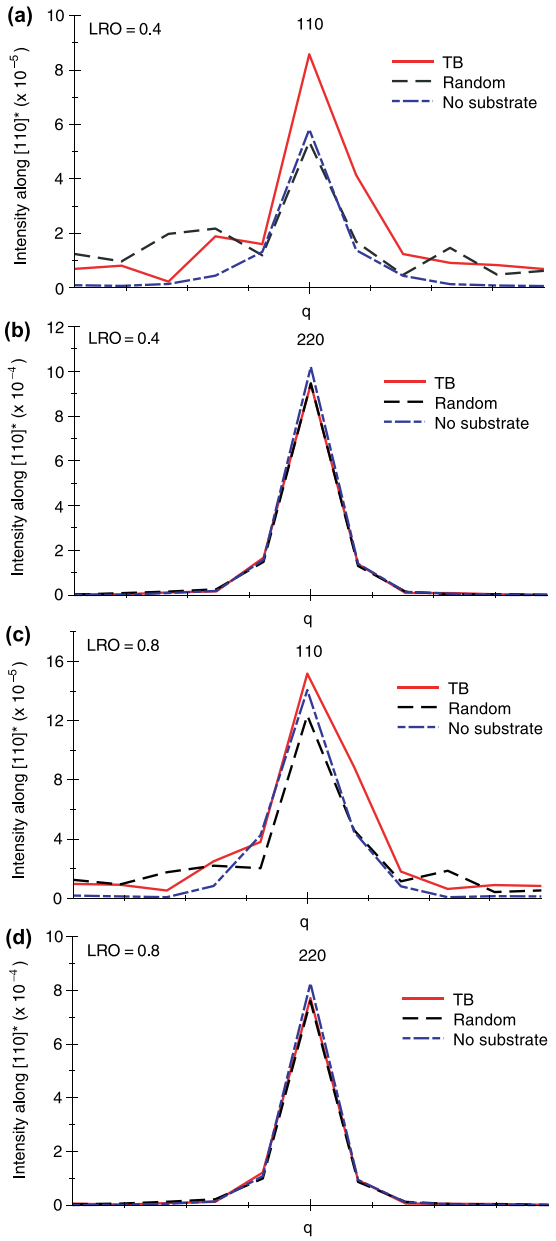

FIG. 4. Intensity profile of the 110 superstructure and the 220 fundamental reflections obtained from the diffraction pattern of a CoPt NP with an long-range order parameter of 0.4 and 0.8 deposited on an amorphous carbon layer simulated by generating random atomic positions and by using the tight-binding approximation: LRO = 0.4: Intensity of the (a) 110 superstructure and (b) 220 fundamental reflections; LRO = 0.8: intensity of the (c) 110 superstructure and (d) 220 fundamental reflections

TABLE II. Values of the intensity of the 110 and 220 reflections and the ratio I_{110}/I_{220} for the NP only, the NP deposited on random carbon and TB carbon, for the 2 values of the LRO parameter, 0.4 and 0.8.

	LRO	I_{110}	I_{220}	I_{110}/I_{220}
NP	0.4	5.82×10^{-5}	1.02×10^{-3}	5.71×10^{-2}
Random	0.4	5.36×10^{-5}	9.46×10^{-4}	5.66×10^{-2}
TB	0.4	8.58×10^{-5}	9.43×10^{-4}	9.10×10^{-2}
NP	0.8	1.41×10^{-4}	8.27×10^{-4}	1.70×10^{-1}
Random	0.8	1.27×10^{-4}	7.60×10^{-4}	1.67×10^{-1}
TB	0.8	1.52×10^{-4}	7.71×10^{-4}	1.97×10^{-1}

For the NP with a LRO parameter of 0.4, the relative difference between the intensity of the 110 reflection on the two carbons is equal to 30% and for the NP with a LRO of 0.8, this difference is equal to 15%.

This result underlines the importance of using a realistic structure for the amorphous substrate when measuring the diffracted peaks of supported NPs, especially in the low spatial frequency range and for weak intensity levels.

The amorphous carbon model generated from random positions of the atoms does not contain any bond length and angle that are present in the TB carbon model. Thus, the diffraction pattern calculated by this model is a uniformly decaying function whose envelope, as a function of the scattering angle, depends on the scattering factor (Fig. 5(a)). At the opposite, the diffraction pattern of the TB carbon contains diffuse scattered rings, as observed experimentally, arising from the 3D atomic arrangement of the C atoms generated by the TB model (Fig. 5(b)). The diffuse scattering intensity at low spatial frequency is evidenced on the radially integrated intensity profile as a function of the scattering vector for both diffraction patterns shown in Fig. 5(c). In consequence, when the NP produces diffracted peaks at low frequencies, their intensity are increased due to the presence of these diffuse rings, as it is the case of the 110 reflection for the CoPt NP in our example.

For interpreting correctly experimental data, it is very important to take into account the effect of the substrate in the measurement of diffracted intensities of supported nano-objects. Indeed, in our case, as it can be seen on Table II, the I_{110}/I_{220} ratios for both LRO values are almost equal for the NP only and for the NP deposited on the random carbon substrate, meaning that the substrate has no effect on the relative values of the diffracted intensities. On the other hand, for the NP deposited on the TB carbon, this ratio is always higher than the one measured on the NP only. This difference is more pronounced for the LRO value of 0.4 since the intensity of the 110 superstructure reflection is weak and thus very sensitive to the diffuse scattering intensity coming from the TB carbon in the low spatial frequency range.

VI. CONCLUSION

In this paper, we have used a tight-binding model to generate a realistic amorphous carbon substrate. By comparison with a simple model of carbon, where the atom positions are generated randomly, we have shown that the limit

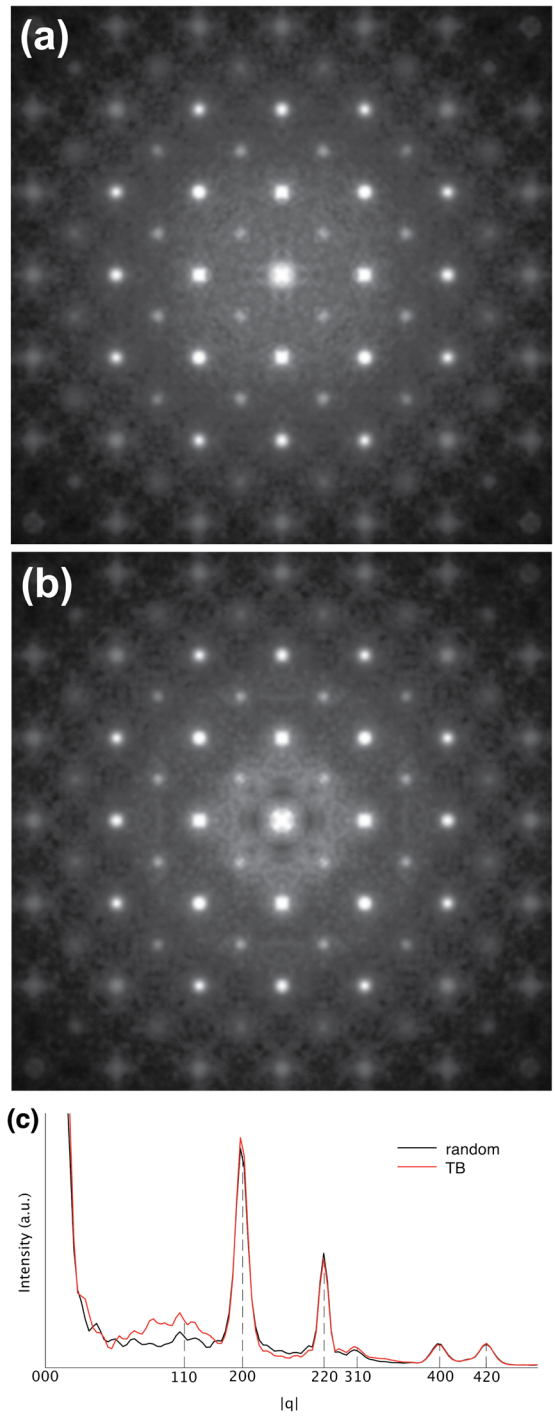

FIG. 5. Electron diffraction calculation of a CoPt NP with a LRO of 0.4 deposited on a 10 nm thick amorphous carbon layer simulated by (a) the random model and (b) the tight-binding model. (c) Radially integrated intensity profile as a function of the scattering vector for both diffraction patterns (a) and (b) in black and red, respectively.

thickness for the weak phase approximation is 30% overestimated if we consider the random carbon model. We have then studied the influence of the carbon model on the contrast of single Cu, Ag, and Au atoms deposited on a-C substrate. Our work does not indicate any significant influence of the carbon structure on single-atom contrast when statistically relevant measurements are performed. Finally, we have compared both model structures of carbon for the determination of the LRO parameter in a small CoPt NP deposited on an a-C layer. We have clearly shown, the importance to use realistic amorphous carbon model to obtain quantitative values for the diffracted intensities. Indeed, diffuse scattering intensity due to the 3D atomic arrangements of the realistic carbon has a significant contribution to the scattered information especially at low spatial frequencies. In a general manner, this work emphasizes the necessity to use realistic carbon model for TEM image simulations in order to extract very sensitive quantitative information, particularly in diffraction experiments.

ACKNOWLEDGMENTS

We wish to acknowledge the financial support of ANR through the DINAMIC project (ANR 11 BS10 009 01).

APPENDIX A: PROPAGATION IN A HOMOGENEOUS ELECTROSTATIC POTENTIAL

The propagation of an electronic wavefunction inside an electrostatic potential $V(r)$ is given by an equation similar to a Schrödinger equation[36]

$$i\frac{d|\Psi\rangle}{dz} = H|\Psi\rangle, \tag{A1}$$

where the Hamiltonian is

$$H = \frac{1}{2k_z}(-\nabla^2 + V(\vec{r})). \tag{A2}$$

∇^2 is the two-dimensional Laplacian and $k_z = \frac{2\pi}{\lambda}$, λ being the electronic wavelength.

The most simple approximation of the electrostatic potential in an amorphous layer is obtained by replacing $V(r)$ by its spatial average $\bar{V}$. In that case, plane waves $|q\rangle$ are eigenfunctions of the new Hamiltonian H_0 with the eigenvalues

$$\gamma_q = \frac{1}{2k_z}(q^2 + \bar{V}). \tag{A3}$$

When considering an incident wave function $|0\rangle$, the propagation of the wavefunction is then

$$|\psi\rangle = \exp(-i\gamma_0 \Delta z)\,|0\rangle. \tag{A4}$$

APPENDIX B: PROPAGATION IN AN INHOMOGENEOUS ELECTROSTATIC POTENTIAL

When considering a slightly inhomogeneous potential, the propagation of the wave function can be estimated by a perturbation expansion. If $\delta V(\vec{r})$ denotes the heterogeneous part of the potential, we have

$$H = H_0 + \delta V(\vec{r}). \tag{B1}$$

Following a classical perturbation scheme,[36] the propagation of an initial plane wave $|0\rangle$ is to the zeroth order given by Eq. (A4). Then, the first order term writes

$$|\psi^{(1)}(z)\rangle = \sum_{q\neq 0} \exp(-i\,\gamma_q\,z) \int_0^z \exp(-i\,(\gamma_q-\gamma_0)\,z') \times \langle q|\delta V(z')|0\rangle\,dz'\;|q\rangle. \tag{B2}$$

Equations (A4) and (B2) can be used to compute the evolution of the transmitted beam intensity. To the second order, calculations leads to

$$I_{q=0} \approx 1 - \langle\psi^{(1)}|\psi^{(1)}\rangle. \tag{B3}$$

This means that the first correction to the energy of the transmitted beam intensity is a decrease due to the intensity diffracted at order 1 on the non zero $|q\rangle$ vectors. Using Eq. (B2), we finally get

$$I_{q=0} \approx 1 - \sum_{q\neq 0} \int_0^z \int_0^z \exp(-i\,(\gamma_q-\gamma_0)\,(z'-z'')) \times \langle q|\delta V(z')|0\rangle\langle q|\delta V(z'')|0\rangle^*\,dz'\,dz'', \tag{B4}$$

where the star denotes the complex conjugate.

1. Inhomogeneous potential case in the projected potential approximation

When considering thin layers, the usual approximation is to replace the potential by its value averaged over the thickness Δz of the layer

$$\delta V(z) \approx \frac{1}{\Delta z}\int_0^{\Delta z} \delta V(z')\,dz' = \frac{\delta V_p^{\Delta z}}{\Delta z}. \tag{B5}$$

Note that the projected potential $\delta V_p^{\Delta z}$ is only a function of $\vec{\rho} = (x, y)$, the two dimensional spatial coordinate perpendicular to z. Under this assumption, Eq. (B3) becomes

$$I_{q=0} \approx 1 - \sum_{q\neq 0} |\langle q|\delta V_p^{\Delta z}|0\rangle|^2 W^{\Delta z}(q), \tag{B6}$$

where

$$W^{\Delta z}(q) = \mathrm{sinc}^2\left(\frac{q^2}{4\,k_z}\,\Delta z\right). \tag{B7}$$

Note that, in an amorphous layer, the Fourier components of the potential $\langle q|\delta V_p^{\Delta z}|0\rangle$ are negligible for large $\vec{q}$ vectors. Then, for thin layers, $W^{\Delta z}(q)$ in Eq. (B6) can be replaced by 1.

2. Fourier components of the projected potential

We now compute the Fourier components of the heterogeneous potential as a function of the carbon atom positions, noted $(\vec{\rho}_i, z_i)$. We introduce the two-dimensional atomic density operator for a layer of thickness Δz:

$$D^{\Delta z}(\vec{\rho}) = \frac{1}{\Delta z}\sum_i \delta(\vec{\rho} - \vec{\rho}_i), \tag{B8}$$

where the sum is extended to all atoms inside the layer and δ is the Dirac function. The density is rescaled so that the integral over the surface layer Ω gives the three dimensional density $\bar{\rho}_0$. The projected potential is

$$V_p^{\Delta z}(\vec{\rho}) = \Delta z \int\int_\Omega D(\vec{\rho}\,')\,\mathcal{V}_p^{at}(\vec{\rho} - \vec{\rho}\,')\,d\vec{\rho}\,', \tag{B9}$$

where $\mathcal{V}_p^{at}$ is the projected potential of a single atom:

$$\mathcal{V}_p^{at}(\vec{\rho}) = \int \mathcal{V}^{at}(\vec{\rho}, z)\,dz. \tag{B10}$$

$\mathcal{V}^{at}(\vec{\rho}, z)$ is the three dimensional potential generated by a single atom. In Eq. (B10), the integration has been extended to infinity because we consider a layer thickness much thicker than the extent of the atomic potential.

Equation (B9) is a convolution, its Fourier transform is thus a simple product. Therefore, considering non zero $|q\rangle$ vectors, we have

$$|\langle q|\delta V_p^{\Delta z}|0\rangle|^2 = (\Delta z)^2\,|\hat{D}^{\Delta z}(q)|^2\,|\hat{\mathcal{V}}_p^{at}(q)|^2. \tag{B11}$$

Introducing the two-dimensional correlation function of atomic positions in the layer

$$\Gamma^{\Delta z}(\vec{\rho}) = \int\int \left(D^{\Delta z}(\vec{\rho}\,') - \bar{\rho}_0\right)\left(D^{\Delta z}(\vec{\rho}\,' + \vec{\rho}) - \bar{\rho}_0\right) d\vec{\rho}\,', \tag{B12}$$

we finally get

$$I_{q=0} \approx 1 - (\Delta z)^2 \sum_{\vec{q}\neq 0} W^{\Delta z}(q)\,\hat{\Gamma}^{\Delta z}(\vec{q})\,|\hat{\mathcal{V}}_p^{at}(q)|^2. \tag{B13}$$

Note that if we consider an isotropic amorphous, the correlation function $\Gamma^{\Delta z}$ only depends on q, the norm of the two-dimensional reciprocal lattice.

3. Scaling of the two-dimensional atomic position correlation function

To reveal how the autocorrelation function $D^{\Delta z}$ depends on the layer thickness Δz, we divide the layer into N sublayers of equal thickness. Introducing the density function D_α of the sublayers α we have

$$D^{\Delta z}(\rho) = \frac{1}{N}\sum_{\alpha=1}^{N} D_\alpha(\rho). \tag{B14}$$

We now assume that the sublayer thickness is significantly larger than the range of the atomic correlation of the three dimensional structure (see the 3D RDF in Fig. 1(c)). Then, atomic positions of atoms belonging to different sublayer are essentially not correlated. Introducing Eq. (B14) in Eq. (B12), we then get

$$\Gamma^{\Delta z}(\vec{\rho}) = \frac{1}{N^2}\sum_{\alpha} \int\int \left(D_\alpha(\vec{\rho}\,') - \bar{\rho}_0\right)\left(D_\alpha(\vec{\rho}\,' + \vec{\rho}) - \bar{\rho}_0\right) d\vec{\rho}\,'. \tag{B15}$$

Because the N sublayers have the same autocorrelation function, we have

$$\Gamma^{\Delta z}(\vec{\rho}) = \frac{1}{N}\,\Gamma^{\Delta z/N}(\vec{\rho}). \tag{B16}$$

We conclude that, as soon as the layer thickness is larger than the three-dimensional correlation distance, the two-dimensional autocorrelation function scales as the inverse of the layer thickness. It means that Eq. (B13) leads to a linear decrease of the transmitted beam intensity with respect to the layer thickness.

[1]D. Alloyeau, T. Oikawa, J. Nelayah, G. Wang, and C. Ricolleau, Appl. Phys. Lett. **101**, 121920 (2012).
[2]D. Alloyeau, B. Freitag, S. Dag, Lin W. Wang, and C. Kisielowski, Phys. Rev. B **80**, 014114 (2009).
[3]B. Gamm, H. Blank, R. Popescu, R. Schneider, A. Beyer, A. Gölzhäuser, and D. Gerthsen, Microsc. Microanal. **18**, 212 (2012).
[4]C. O. Girit, J. C. Meyer, R. Erni, M. D. Rossell, C. Kisielowski, L. Yang, C.-H. Park, M. F. Crommie, M. L. Cohen, S. G. Louie, and A. Zettl, Science **323**, 1705 (2009).
[5]C. Kisielowski, Q. M. Ramasse, L. P. Hansen, M. Brorson, A. Carlsson, A. M. Molenbroek, H. Topsoe, and S. Helveg, Angew. Chem., Int. Ed. **49**, 2708 (2010).
[6]D. Alloyeau, C. Ricolleau, T. Oikawa, C. Langlois, Y. Le Bouar, and A. Loiseau, Ultramicroscopy **109**, 788–796 (2009).
[7]M. Valamanesh, C. Langlois, D. Alloyeau, E. Lacaze, and C. Ricolleau, Ultramicroscopy **111**, 149–154 (2011).
[8]P. L. Gai, M. J. Goringe, and J. C. Barry, J. Microscopy **142**, 9 (1986).
[9]H. Schultrich and B. Schultrich, Ultramicroscopy **88**, 111 (2001).
[10]O. L. Krivanek, P. H. Gaskell, and A. Howie, Nature **262**, 454 (1976).
[11]J. P. Chevalier and M. J. Hytch, Ultramicroscopy **52**, 253 (1993).
[12]C. B. Boothroyd, Ultramicroscopy **83**, 159 (2000).
[13]J. M. Gibson, Ultramicroscopy **56**, 26 (1994).
[14]H. S. Baik, T. Epicier, and E. Van Cappellen, Eur. Phys. J.: Appl. Phys. **4**, 11 (1998).
[15]M. M. J. Treacy and J. M. Gibson, Acta Crystallogr., Sect. A: Cryst. Phys., Diffr., Theor. Gen. Crystallogr. **52**, 212 (1998).
[16]H. Amara, J. M. Roussel, J. P. Gaspard, C. Bichara, and F. Ducastelle, Phys. Rev. B **79**, 014109 (2009).
[17]F. H. Stillinger and T. A. Weber, Phys. Rev. B **31**, 5262 (1985).
[18]N. A. Marks, Phys. Rev. B **63**, 035401 (2000).
[19]J. Tersoff, Phys. Rev. Lett. **56**, 632 (1986).
[20]J. Tersoff, Phys. Rev. Lett. **61**, 2879 (1988).
[21]J. H. Los, L. M. Ghiringhelli, E. J. Meijer, and A. Fasolino, Phys. Rev. B **72**, 214102 (2005).
[22]A. C. T. van Duin, S. Dasgupta, F. Lorant, and W. A. Goddard III, J. Phys. Chem. A **105**, 9396 (2001).
[23]C. H. Xu, C. Z. Wang, C. T. Chan, and K. M. Ho, J. Phys.: Condens. Matter **4**, 6047 (1992).
[24]D. Porezag, Th. Frauenheim, Th. Kohler, G. Seifert, and R. Kaschner, Phys. Rev. B **51**, 12947 (1995).
[25]D. G. Pettifor and I. I. Oleinik, Phys. Rev. B **59**, 8487 (1999).
[26]R. Haydock, V. Heine, and M. J. Kelly, J. Phys. C **5**, 2845 (1972).
[27]D. Frenkel and B. Smit, *Understanding Computer Simulation* (Academic Press, London, 1996).
[28]J. H. Los, C. Bichara, and R. J. M. Pellenq, Phys. Rev. B **84**, 085455 (2011).
[29]D. R. McKenzie, D. Muller, and B. A. Pailthorpe, Phys. Rev. Lett. **67**, 773 (1991).
[30]S. K. Jain, R. J.-M. Pellenq, J. P. Pikunic, and K. E. Gubbins, Langmuir **22**, 9942 (2006).
[31]See supplementary material at http://dx.doi.org/10.1063/1.4831669 for downloading the.xyz files that contain the carbon atomic positions of the amorphous carbon blocks generated by using the tight-binding model.
[32]P. A. Stadelmann, Ultramicroscopy **21**, 131 (1987).
[33]E. J. Kirkland, *Advanced Computing in Electron Microscopy* (Springer, 2009).
[34]L.-M. Peng, G. Ren, S. L. Dudarev, and M. J. Whelan, Acta Crystallogr., Sect. A: Cryst. Phys., Diffr., Theor. Gen. Crystallogr. **52**, 257 (1996).
[35]C. Ricolleau, J. Nelayah, T. Oikawa, Y. Kohno, N. Braidy, G. Wang, F. Hue, and D. Alloyeau, JEOL News **47**, 2 (2012); available at http://www.jeolusa.com/NEWSEVENTS/JEOLNEWSMagazine/tabid/275/Default.aspx.
[36]D. Gratias and R. Portier, Acta Crystallogr., Sect. A: Cryst. Phys., Diffr., Theor. Gen. Crystallogr **39**, 576 (1983).
[37]D. Alloyeau, G. Prévot, Y. Le Bouar, T. Oikawa, C. Langlois, A. Loiseau, and C. Ricolleau, Phys. Rev. Lett. **105**, 255901 (2010).
[38]I. M. Lifshitz and V. V. Slyozov, J. Phys. Chem. Solids **19**, 35 (1961).
[39]C. Wagner, Z. Elektrochem. **65**, 581 (1961).
[40]D. Alloyeau, C. Langlois, C. Ricolleau, Y. Le Bouar, and A. Loiseau, Nanotechnol. **18**, 375301 (2007).
[41]W. W. Pai, A. K. Swan, Z. Zhang, and J. F. Wendelken, Phys. Rev. Lett. **79**, 3210 (1997).
[42]M. Zinke-Allmang, L. C. Feldman, and M. H. Grabow, Surf. Sci. Rep. **16**, 377 (1992).
[43]G. Palasantzas, T. Vystavel, S. A. Koch, and J. T. M. De Hosson, J. Appl. Phys. **99**, 024307 (2006).
[44]A. Rose, *Advances Electronics and Electron Physics* (Academic Press, New York, 1948).
[45]N. Blanc, F. Tournus, V. Dupuis, and T. Epicier, Phys. Rev. B **83**, 092403 (2011).
[46]K. Sato, Y. Hirotsu, H. Mori, Z. Wang, and T. Hirayama, J. Appl. Phys. **97**, 084301 (2005).
[47]K. Sato, Y. Hirotsu, H. Mori, Z. Wang, and T. Hirayama, J. Appl. Phys. **98**, 024308 (2005).
[48]T. Miyazaki, O. Kitakami, S. Okamoto, Y. Shimada, Z. Akase, Y. Murakami, D. Shindo, Y. K. Takahashi, and K. Hono, Phys. Rev. B **72**, 144419 (2005).
[49]D. Alloyeau, C. Ricolleau, C. Mottet, T. Oikawa, C. Langlois, Y. Le Bouar, N. Braidy, and A. Loiseau, Nature Mater. **8**, 940 (2009).
[50]L. Castaldi, K. Giannakopoulos, A. Travlos, D. Niarchos, S. Boukari, and E. Beaurepaire, J. Magn. Magn. Mater. **290–291**, 544 (2005).
[51]Y. Sui, L. Yue, R. Skomski, X. Z. Li, J. Zhou, and D. J. Sellmyer, J. Appl. Phys. **93**, 7571 (2003).
[52]G. Rossi, R. Ferrando, and C. Mottet, Faraday Discuss. **138**, 193 (2008).
[53]P. Moskovkin, S. Pisov, M. Hou, C. Raufast, F. Tournus, L. Favre, and V. Dupuis, Eur. Phys. J. D **43**, 27 (2007).
[54]A. Kashyap, K. B. Garg, A. K. Solanki, T. Nautiyal, and S. Auluck, Phys. Rev. B **60**, 2262 (1999).
[55]S. Karoui, H. Amara, B. Legrand, and F. Ducastelle, J. Phys.: Condens. Matter **25**, 056005 (2013).